



Transport and electrochemical properties of high potential tavorite LiVPO₄F

P.F. Xiao, M.O. Lai, L. Lu *

Materials Science Group, E3-04-01, 2 Engineering Drive 3, National University of Singapore, 117581 Singapore, Singapore



ARTICLE INFO

Article history:

Received 22 January 2013

Received in revised form 4 April 2013

Accepted 7 April 2013

Available online 3 May 2013

Keywords:

Lithium-ion batteries
Cathode
Tavorite structure
Conductivity
Diffusion coefficient

ABSTRACT

Tavorite-structured 4 V-class LiVPO₄F as a safe and durable cathode material for lithium-ion batteries (LIBs) has been studied. The electrical transport and ionic diffusion properties of LiVPO₄F at different temperature and at different charge-discharge states have been systematically investigated for the first time. At room temperature, LiVPO₄F shows a relatively high bulk ionic conductivity of $\sim 8 \times 10^{-7}$ S cm⁻¹ but a poor electronic conductivity of $\sim 10^{-11}$ S cm⁻¹. This work uncovers an abnormal non-Arrhenius temperature dependence of electrical conductivity in the temperature range of 30–90 °C for tavorite LiVPO₄F. Li⁺ diffusivity of Li_{1-x}VPO₄F ($0 \leq x \leq 1$) at different delithiated/lithiated states and have been comprehensively studied for the first time, through galvanostatic charge-discharge, galvanostatic intermittent titration technique (GITT), electrochemical impedance spectroscopy (EIS) and cyclic voltammetry (CV). The electronic insulating nature may be the main bottleneck towards high rate performances for LiVPO₄F at room temperature. To tackle this challenge, the strategy of carbon coating has been adopted in this work. The LiVPO₄F/C composite exhibits impressive rate capability and good long-term cyclability at both room temperature and elevated temperature (55 °C).

© 2013 Elsevier B.V. All rights reserved.

1. Introduction

Lithium-ion batteries (LIBs) have already dominated the market for electronic devices and are moving towards large-scale applications such as power tools, hybrid/electric vehicles (HEVs/EVs) and even smart grid. Phosphate-based materials have been extensively studied and developed as safe and durable cathodes for large-scale LIBs for the past decade. In particular, olivine-structured LiFePO₄ has been widely recognized as one of the most promising cathode materials for electric vehicles (EVs) and hybrid vehicles (HEVs). However, its low potential (3.4 V vs. Li⁺/Li) is an intrinsic drawback to the urgent eager for high power/energy density. To overcome this problem, many efforts have been devoted to explore new polyanion materials with higher potential and/or higher capacity [1–4]. Tavorite-structured fluorophosphates LiMPO₄F and Li₂MPO₄F (M = Fe, Mn, Co, Ti etc.) [5,6] and fluorosulphates LiMSO₄F (M = Fe, Ni, Co, Mn etc.) [3,4] receive increasing research attention recently.

Tavorite LiVPO₄F, firstly proposed by Barker et al. [7], has a relatively high potential of 4.2 V (vs. Li⁺/Li) and a theoretical capacity of 155 mA h g⁻¹ from a one-electron V³⁺/V⁴⁺ redox. As a “4 V-class” cathode material, LiVPO₄F is electrochemically more active than its direct competitor LiMnPO₄ (4.1 V vs. Li⁺/Li) in the olivine family [8,9]. Unlike other 4 V cathode materials [10–12], LiVPO₄F shows excellent lattice stability, good thermal stability with electrolyte and good long-term cyclic performance owing to the consolidus covalent-bonded crystal structure. Differential scanning calorimetry (DSC) test showed that LiVPO₄F in a charged state is thermally stable up to 175 °C, as good as olivine LiFePO₄,

the most thermal-stable cathode material known so far [13,14]. Good cyclic performances at room temperature have been demonstrated both in half-cells and in full-cells when coupling with graphite anode [15,16].

Although tavorite LiVPO₄F has exhibited promising electrochemical properties, some fundamental properties of this material have not been thoroughly studied until now. Therefore, the present work has been focused on the intrinsic electrical transport, ionic diffusivity and Li⁺ extraction/insertion mechanisms of tavorite LiVPO₄F. This work may bring new insights of this category of electrode materials and may pave a way for further optimization and research.

Similar to most of the phosphate-based materials, electronic transport in tavorite LiVPO₄F lattice is expected to be inferior when compared to conventional oxide cathode materials. Most of the previous reports adopted solid-state reaction with the assistance of carbon thermal reduction to obtain LiVPO₄F/C composite, since it is difficult to obtain pure-phase LiVPO₄F through wet-chemistry routes due to the light and sensitive fluoride. Herein, pristine and carbon coated LiVPO₄F were synthesized via an optimized conventional solid-state reaction using hydrogen and acetylene carbon black as reduction agent, respectively.

2. Experimental

2.1. Material preparation

Pristine carbon-free LiVPO₄F was synthesized via a two-step solid-state reaction assisted with hydrogen thermal reduction (HTR). Raw materials of vanadium oxide (V₂O₅, 99%, 0.01 mol) and dihydrogen phosphate (NH₄H₂PO₄, 99%, 0.02 mol) were milled for 2 h without any additives using a SPEX-8000 M high-energy milling machine. Stainless

* Corresponding author. Tel.: +65 65162236; fax: +65 67791459.

E-mail address: luli@nus.edu.sg (L. Lu).

steel jar and balls were used as milling media. Reduction of V^{5+} to V^{3+} was achieved by heating the powder mixture at 700 °C in flowing forming gas (5 vol.% H₂ in Ar). The pre-calculated VPO₄ powder was mixed with stoichiometric excessive (2 wt.%) lithium fluoride (LiF, 99%) through high-energy ball milling. Gray green colored LiVPO₄F powder was finally obtained after a rapid calcination at 700 °C in argon.

Carbon coated LiVPO₄F (LiVPO₄F/C) was synthesized via a similar solid-state reaction assisted with carbon thermal reduction (CTR). Raw materials of V₂O₅ (0.01 mol), NH₄H₂PO₄ (0.02 mol) and acetylene carbon black (0.36 g) were ball milled for 2 h. A small amount of stearic acid (3 wt.%) was added as processing control agent to improve the milling efficiency. The mixed powder was calcined at 700 °C for 12 h in flowing argon to obtain VPO₄/C precursor. The pre-calculated VPO₄/C powder was then milled again with LiF. Black LiVPO₄F/C powder was finally obtained after a rapid calcination at 700 °C in flowing argon.

2.2. Characterization

Crystal structure was characterized using step-scan powder X-ray diffraction (XRD, Shimadzu XRD-6000, Cu-K α radiation) with a step width of 0.02° and a duration of 4 s per step. Scanning electron microscope (SEM, Hitachi S-4300) and transmission electron microscope (TEM, JEM2010F) were used for morphological and microstructural characterization. Residual carbon content in LiVPO₄F/C was determined through elemental analysis and thermogravimetric analysis (TGA).

Total electrical conductivity and electronic conductivity were measured using alternating-current (AC) impedance spectroscopy and direct-current (DC) polarization with Solartron 1287 + 1260 electrochemistry system. Dense ceramic pellets of carbon free LiVPO₄F were prepared using the hydrogen thermal reduction method. The as-milled power mixture of VPO₄ and LiF was compacted in a stainless steel die with a pressure of 250 MPa before the final calcination. A typical disk pellet of LiVPO₄F is of ~10 mm in diameter and ~1 mm in thickness with a density ~80% of the theoretical value. Both faces of the as-sintered disk ceramic pellet were carefully ground and polished. Gold or platinum were sputtered on both faces as ionic blocking electrodes. As a comparison, extrinsic electronic conductivity of the LiVPO₄F/C composite was also measured using compacted powder. The LiVPO₄F/C powder was compacted in a Swagelok Teflon cell of 12.5 mm in diameter by cylinder electrodes made of stainless steel under a pressure of 250 MPa.

2.3. Electrochemical test

Working electrodes were prepared by doctor-blade method. The active material, carbon black (Super P) and polyvinylidenefluoride (PVDF, 99%, Sigma-Aldrich) were thoroughly mixed in a weight ratio of 80: 15: 5 in the solvent of n-methyl-2-pyrrolidone (NMP). The as-mixed viscous slurry was then pasted on aluminum foils to obtain working electrodes. The loading density of active LiVPO₄F was controlled to be ~4 mg cm⁻². After pre-drying, working electrodes were pressed by a rolling machine and then thoroughly dried at 120 °C in vacuum for 12 h before battery assembly. Swagelok type two-electrode half-cells were assembled in a glove box filled with argon. One Celgard 2500 separator was sandwiched by a working electrode and a 0.59 mm thick metallic lithium foil. The electrolyte was 1 M LiPF₆ in ethylene carbonate (EC), diethyl carbonate (DEC) and dimethyl carbonate (DMC) solutions (EC:DEC:DMC, 1:1:1 in volume).

Electrochemical characterizations were carried out at room temperature (25 °C) and elevated temperatures (40 °C and 55 °C). Galvanostatic charge-discharge cycling tests were carried out between 3.0 V and 4.6 V using MacCor 4304 and Neware BTS-5V1A. Galvanostatic intermittent titration technique (GITT), electrochemical impedance spectroscopy (EIS) and cyclic voltammetry (CV) tests were carried out using Solartron 1400 cell system. GITT was carried out with a current pulse of 37.5 mA g⁻¹ (0.25 C) for 300 s followed by a relaxation at open circuit for 90 min in

each step. EIS was carried out with a 5 mV amplitude vs. open circuit potential (OCP) within frequency range from 1 MHz to 1 mHz. Prior to each EIS test, the cell was held at open circuit for 4 h to achieve the quasi-equilibrium state.

3. Results and discussion

3.1. Characterization

3.1.1. Crystal structure

Fig. 1(a) shows XRD spectra and Rietveld refinement of carbon free LiVPO₄F and the LiVPO₄F/C composite. Both materials show similar diffraction patterns of P-1 triclinic phase. The excessive LiF added in the milling process compensated for the loss of fluorine and lithium during calcination, which successfully prevented the Li₃V₂(PO₄)₃ impurity phase frequently reported before [14,15]. Rietveld refinement was carried out using GSAS + EXPGUI [17,18] to further characterize the crystal structure. Starting crystal structure in the refinement was set after the report on isomorph LiFePO₄F [5]. The refined pattern fits very well with the crystal structure of amblygonite LiAlPO₄F and tavorite LiFePO₄(OH). As shown in Table 1, the refined atomic parameters are consistent with previous reports [15,19], while atomic parameters of carbon free LiVPO₄F and LiVPO₄F/C are almost identical. With a cell volume of 174.6 Å³, the theoretical density of LiVPO₄F can be calculated to be 3.274 g cm⁻³, slightly lower than those of olivine LiFePO₄ (3.5 g cm⁻³) and LiMnPO₄ (3.4 g cm⁻³). In the tavorite lattice of LiVPO₄F, VO₄F₂ octahedrons are linked with corner sharing F⁻ ion in one-dimensional zig-zag chains. The chains of VO₄F₂ octahedron are further cross-linked by PO₄ tetrahedrons, forming a 3-D framework. Transitional metal ions V³⁺ are separated either by corner sharing electronegative F⁻ or covalent-bonded PO₄ tetrahedrons, leading to a poor one-dimensional hopping conduction. Li⁺ ions are located in severely disordered octahedrons and are split into two sites with a distance of ~0.7 Å, similar to the case of amblygonite LiAlPO₄F and LiFePO₄F [5]. In contrast to the 1-D Li⁺ migration in the olivine lattice of LiMPO₄ (M = Fe, Mn, etc.), tavorite lattice provides 3-D diffusion tunnels for Li⁺. The most probable diffusion

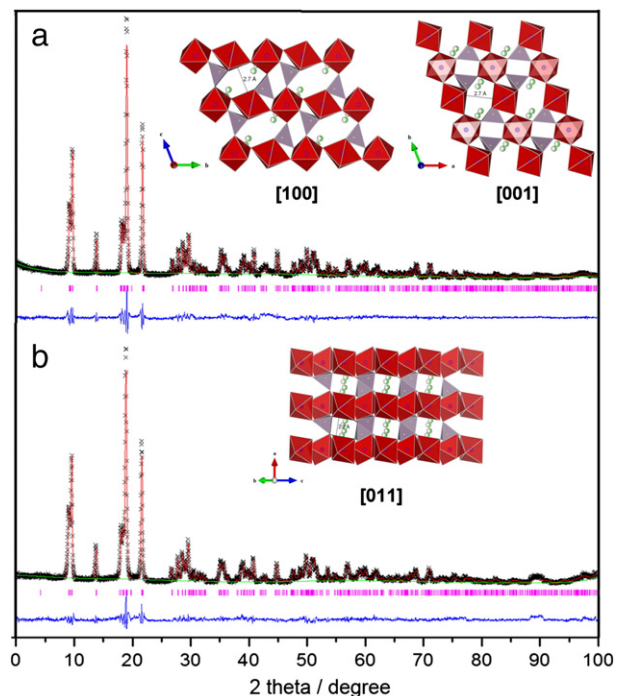


Fig. 1. XRD spectra and Rietveld refinement of (a) pristine LiVPO₄F (b) LiVPO₄F/C. Insets are possible Li⁺ migration tunnels in the lattice of tavorite LiVPO₄F.

Table 1XRD Rietveld refinement results and atomic parameters of LiVPO₄F.

Atom	x	y	z	Occupancy	R_{wp}	R_p	CHI^2	R_{wp}	R_p	CHI^2	
											U_{iso}
LiVPO ₄ F-HTR	$a = 5.3115(2)$ Å		$\alpha = 107.934(3)$ °		$V = 174.62$ Å ³		$R_{wp} = 10.06\%$		$R_p = 7.58\%$		$\text{CHI}^2 = 3.420$
LiVPO ₄ F/C-CTR	$b = 7.2617(2)$ Å		$\beta = 98.444(3)$ °		$V = 174.56$ Å ³		$R_{wp} = 11.37\%$		$R_p = 8.66\%$		$\text{CHI}^2 = 3.748$
	$c = 5.1744(2)$ Å		$\gamma = 107.547(3)$ °								
	$a = 5.3104(3)$ Å		$\alpha = 107.950(5)$ °								
	$b = 7.2636(4)$ Å		$\beta = 98.404(4)$ °								
	$c = 5.1731(3)$ Å		$\gamma = 107.573(4)$ °								
Li1	0.625(7)	0.301(7)	0.250(9)	0.5							0.019
Li2	0.612(6)	0.211(6)	0.266(7)	0.5							0.019
V1	0	1/2	0	1							0.025(2)
V2	0	0	0	1							0.019(2)
P	0.6495(10)	0.7532(10)	0.3283(11)	1							0.015(1)
O1	0.6655(15)	0.8534(16)	0.1055(21)	1							0.025(3)
O2	0.3613(21)	0.6406(14)	0.3175(19)	1							0.016(2)
O3	0.7985(18)	0.5978(15)	0.2645(17)	1							0.020(3)
O4	0.2407(17)	0.0966(15)	0.3678(21)	1							0.019(3)
F	0.9201(14)	0.2554(14)	0.1159(15)	1							0.012(3)

tunnels lie along [001], [100] and [011], as shown in the insets of Fig. 1 (built with VESTA [20] software).

3.1.2. Conductivity

The total electrical conductivity of bulk LiVPO₄F was measured using impedance spectroscopy with ionic-blocking disk specimens of Au/LiVPO₄F/Au. The measured electrical conductivity denoted as σ_{AC} was contributed from both electronic and ionic transport. As shown in Fig. 2(a), σ_{AC} of LiVPO₄F is 8.1×10^{-7} S cm⁻¹ at room

temperature, which is notably higher than those of isomorph LiFeSO₄F (7.0×10^{-11} S cm⁻¹ [3]) and olivine LiFePO₄ (1.39×10^{-9} S cm⁻¹ [9]). The straight line tail in the low frequency range of the Cole–Cole plot evidently indicates a strong ionic diffusion, similar to the report [3] of isomorph LiFeSO₄F. Therefore, the ionic transport should be dominant in favorite LiVPO₄F lattice at room temperature, in contrast to the electronic dominated mechanism in olivine lattice.

Fig. 2(b) to (d) shows the Cole–Cole plots of impedance spectroscopy recorded at various temperatures from -30 to 130 °C, while the

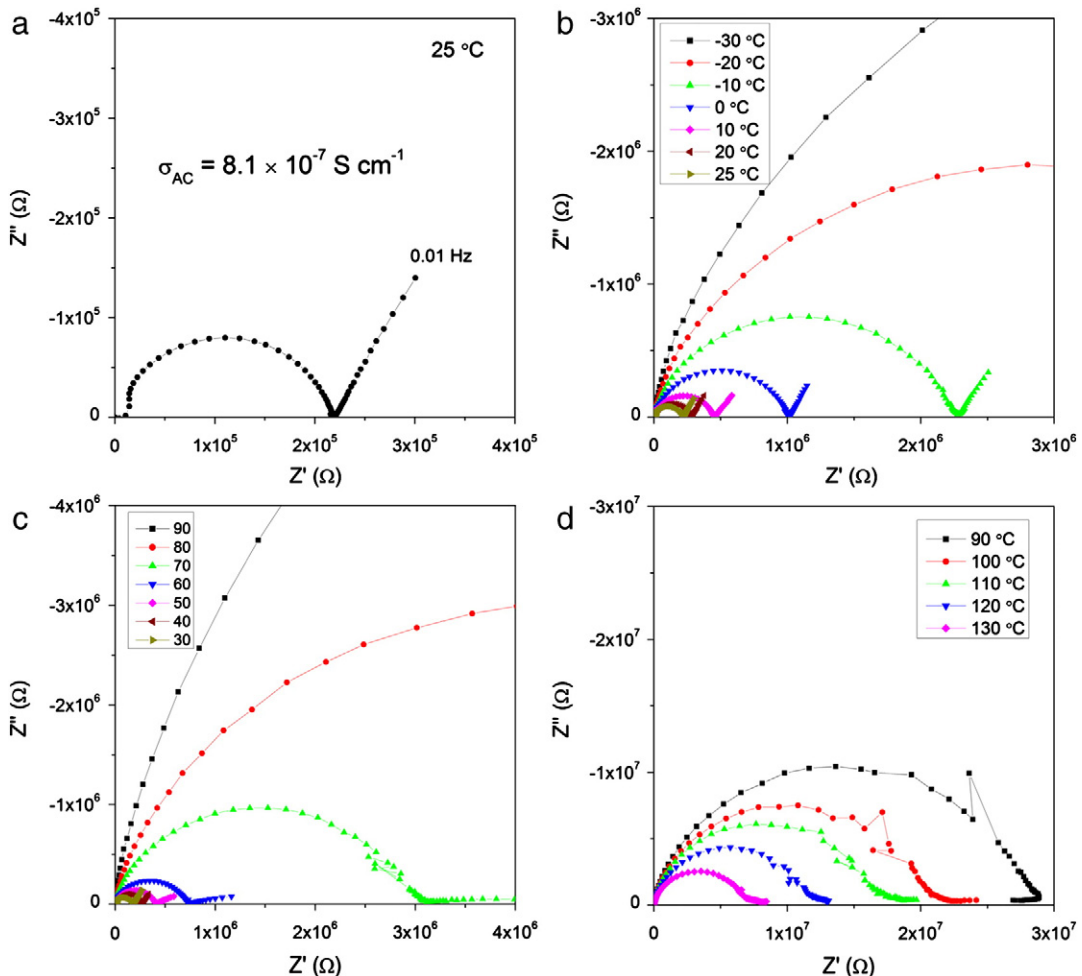


Fig. 2. Cole–Cole plots of impedance spectroscopy of Au/LiVPO₄F/Au specimen at (a) room temperature (25 °C), (b) -30 – 25 °C, (c) 30 – 90 °C and (d) 90 – 130 °C.

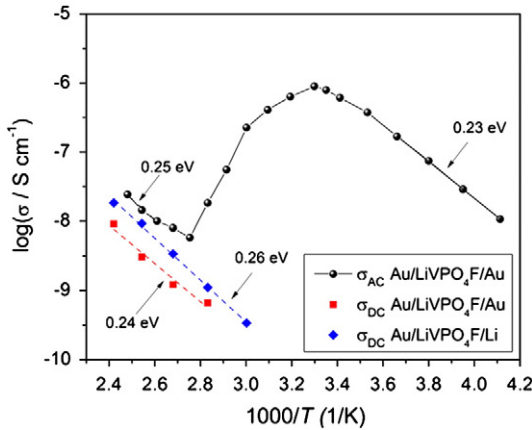


Fig. 3. Temperature dependence of the measured σ_{AC} and σ_{DC} of LiVPO₄F.

temperature dependence of σ_{AC} is further summarized in Fig. 3. As well known, the conductivity of cathode materials normally increases with temperature following Arrhenius equation: $\sigma \propto \exp(-\Delta E / k_B T)$, where k_B is Boltzmann constant, T is the absolute temperature and ΔE is known as activation energy. σ_{AC} increases with temperature in the ranges of -30 – 30 °C and 90 – 130 °C, which agrees well with the Arrhenius equation. The activation energy ΔE for $T > 90$ °C and $-30 \leq T \leq 30$ °C can be calculated to be 0.25 eV and 0.23 eV, respectively. However, σ_{AC} of LiVPO₄F exhibits abnormal temperature dependence in the range of 30 – 90 °C. As can be seen, σ_{AC} declines by more than 2 orders of magnitude and then reaches the bottom at ~ 90 °C. Since the ionic conductivity is supposed to be the major part of σ_{AC} , this phenomenon should be

more related to the change of ionic transport rather than electronic conductivity. As shown in Fig. 2(c), the slope of the straight line tail that is driven by ionic diffusion declines gradually in temperature range of 30 – 90 °C. This is obviously different from the conductivity decrease for $T < 25$ °C as shown in Fig. 2(b). Furthermore, the diffusion tail finally fades away at 90 °C, showing an electronic dominant transport behavior. Although the detailed mechanism of this abnormal temperature dependence of electrical conductivity is still not very clear at this moment, we speculate that a second-order phase transition might take place, which may largely alter the distribution of Li⁺ in split sites and therefore greatly impairs ionic conduction. Further verifications and deep investigations on this interesting phenomenon are now still ongoing.

Electronic conductivity σ_{DC} of bulk LiVPO₄F was derived through direct-current (DC) polarization using ionic-blocking disk specimens of Au/LiVPO₄F/Au. The electronic conductivity was also measured following Hebb-Wagner (H-W) method [21] using Au/LiVPO₄F/Li specimens, as the impedance spectroscopy suggests that the electrons should be minor charge carriers when compared to ions at room temperature. The measured σ_{DC} are shown in Fig. 3. σ_{DC} is very close to σ_{AC} for $T > 90$ °C, supporting our deduction that ionic conduction loses its ascendancy for $T > 90$ °C. The activation energy for σ_{DC} obtained from ionic-blocking method and the H-W method is 0.24 eV and 0.26 eV respectively, also approximate to that (0.25 eV) obtained from σ_{AC} .

The σ_{DC} results imply a low electronic conductivity of only $\sim 10^{-11}$ S cm⁻¹ at room temperature, considerably lower than that of olivine LiFePO₄ (1.78×10^{-9} S cm⁻¹ [9]) and far lower than those of oxide cathode materials such as LiCoO₂ ($\sim 10^{-3}$ – 10^{-1} S cm⁻¹ [22]) and LiMn₂O₄ ($\sim 10^{-5}$ – 10^{-4} S cm⁻¹ [23]). The conductivity results suggest that tavorite LiVPO₄F should be an electronic insulator but a

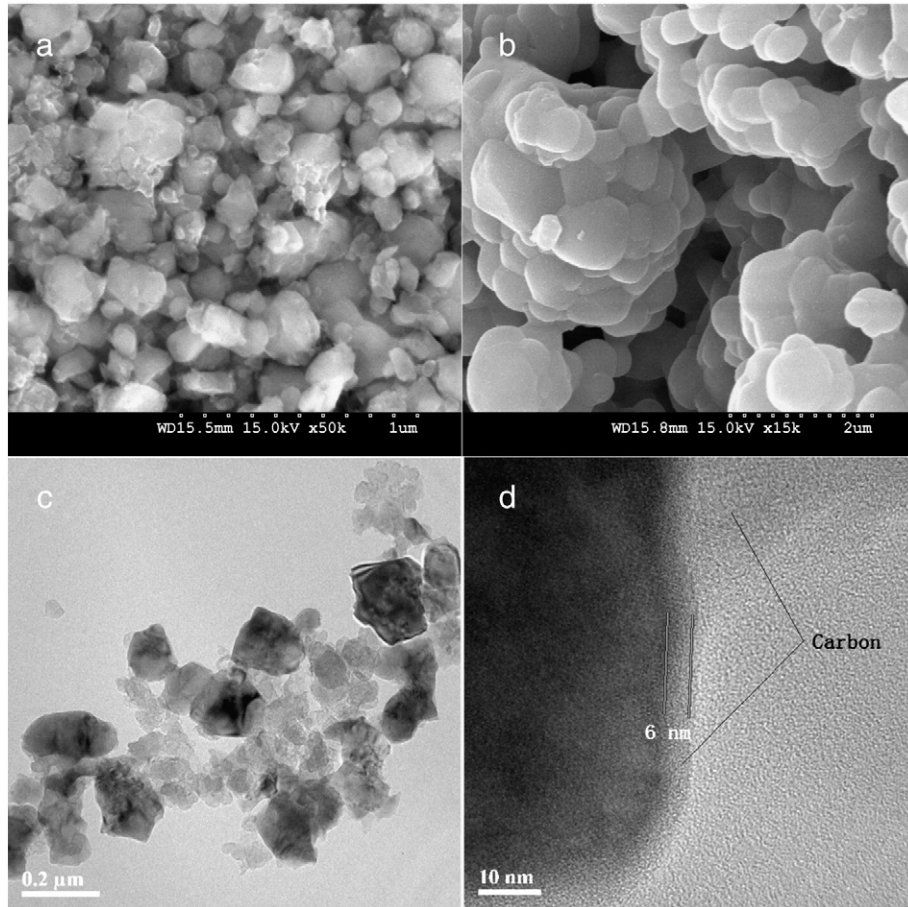


Fig. 4. Micro-morphologies of LiVPO₄F/C composite and pure LiVPO₄F. (a) SEM image of LiVPO₄F/C, (b) SEM image of pLiVPO₄F and (c, d) TEM images of LiVPO₄F/C.

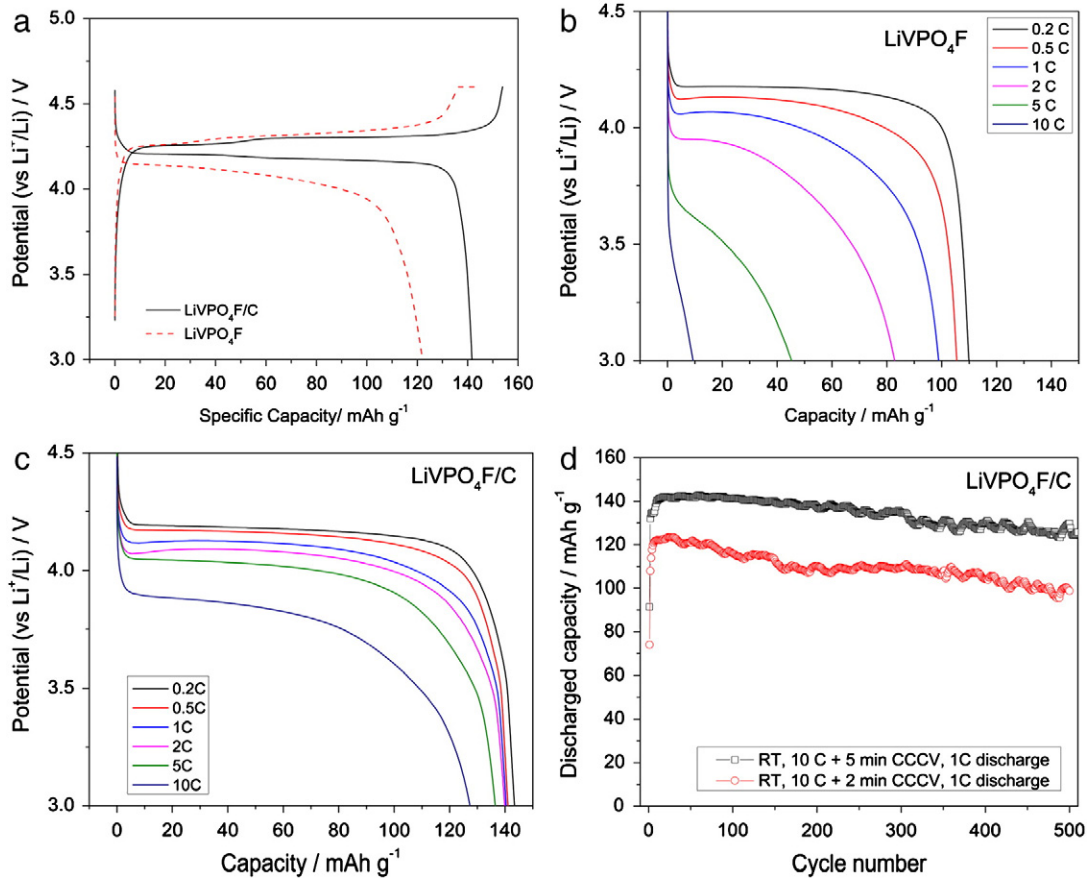


Fig. 5. Galvanostatic charge–discharge properties of LiVPO₄F and LiVPO₄F/C half-cells at room temperature (25 °C). (a) 0.1C charge–discharge profile of LiVPO₄F and LiVPO₄F/C, (b) discharge rate capabilities of LiVPO₄F, (c) discharge rate capabilities of LiVPO₄F/C, and (d) cyclic performance of LiVPO₄F/C.

relatively fast Li⁺ ionic conductor at room temperature, in consistence with the crystal structure analysis. This electronic insulating nature will doubtlessly hinder the electrochemical reaction for the pristine LiVPO₄F. On the other hand, the LiVPO₄F/C composite has a matrix electronic conductivity of 6.5×10^{-2} S cm⁻¹ at room temperature, 6 orders higher than that of carbon-free LiVPO₄F. Although this value does not reflect the intrinsic electronic conductivity, it still suggests a greatly improved electronic transport of LiVPO₄F/C as in practical electrodes.

3.1.3. Micromorphology

The residual carbon content in the LiVPO₄F/C composite was determined to be 8.1 wt.% by elemental analysis and further confirmed to be 9 wt.% by thermogravimetric analysis. Fig. 4 shows SEM and TEM images of LiVPO₄F/C and pristine LiVPO₄F. Carbon additives have successfully impeded the grain growth and particle coarsening during calcination. The particle size of LiVPO₄F/C (~200 nm) is evidently smaller than that of carbon-free LiVPO₄F (~400 nm). Moreover, the serious particle agglomeration as in carbon-free LiVPO₄F was also relieved by well dispersed residual carbon in LiVPO₄F/C. As shown in the high-resolution TEM image of Fig. 3(d), the LiVPO₄F particle is well wrapped by amorphous carbon layer ~6 nm thick.

3.2. Electrochemical properties

3.2.1. Galvanostatic charge–discharge

Battery performances of LiVPO₄F as cathode material were characterized through galvanostatic charge–discharge. Fig. 5(a) shows the first cycle 0.1C (15 mA g⁻¹) charge–discharge profiles of LiVPO₄F and LiVPO₄F/C half-cells at room temperature. With prolonged constant voltage charge to 0.02 C, the initial charge capacity of carbon-free LiVPO₄F can reach 147 mA h g⁻¹, while only 122 mA h g⁻¹ can be

reversibly discharged. On the other hand, LiVPO₄F/C has a higher initial charge capacity of 153 mA h g⁻¹ and a higher reversible discharge capacity of 142 mA h g⁻¹. The voltage hysteresis between charge and discharge plateaus of the LiVPO₄F/C composite is also noticeably narrower than that of carbon-free LiVPO₄F, as a result of the better electronic transport and the smaller particle size.

Fig. 5(b) and (c) shows discharge rate capabilities of the carbon-free LiVPO₄F and LiVPO₄F/C. Half-cells were charged to 4.6 V and then directly discharged to 3 V in a constant current (CC) mode. Carbon-free LiVPO₄F can deliver a capacity of 110 mA h g⁻¹ at 0.2 C, while only 40% and 8% of its 0.2 C specific capacity can be achieved at 5 C and 10 C, respectively. The main reason for the sluggish rate performance should be the poor electronic conductivity of LiVPO₄F. On the other hand, the LiVPO₄F/C composite delivers high specific capacity of 142 mA h g⁻¹ at 0.2 C and shows impressive high-rate performance. For example, 137 mA h g⁻¹ (96% of its 0.2 C specific capacity) can still be discharged at 5 C, while 127 mA h g⁻¹ (89% of its 0.2 C specific capacity) can be discharged at 10 C. LiVPO₄F/C shows greatly improved rate capability due to the largely enhanced electronic transport and the smaller particle size. This good rate capability was achieved without harsh control of particle size and complex processing, owing to the intrinsically fast ionic transport in the lattice of favorite LiVPO₄F.

LiVPO₄F/C is also capable of fast charge, which is a very favorable feature in practical applications. The LiVPO₄F/C half-cells can be charged to more than 80% state of charge (SOC) at 10 C (about 5 min). Cyclic tests in constant current–constant voltage (CCCV) charge mode were carried out to further characterize its long-term stability along with fast charge. Fig. 5(d) shows the discharged capacity as a function of cycle number in the cyclic tests. In this CCCV mode, cells were charged at a constant current of 10 C to 4.5 V and then charged for an additional 5 min or 2 min, therefore the total charging time in each cycle was about ~10 min and

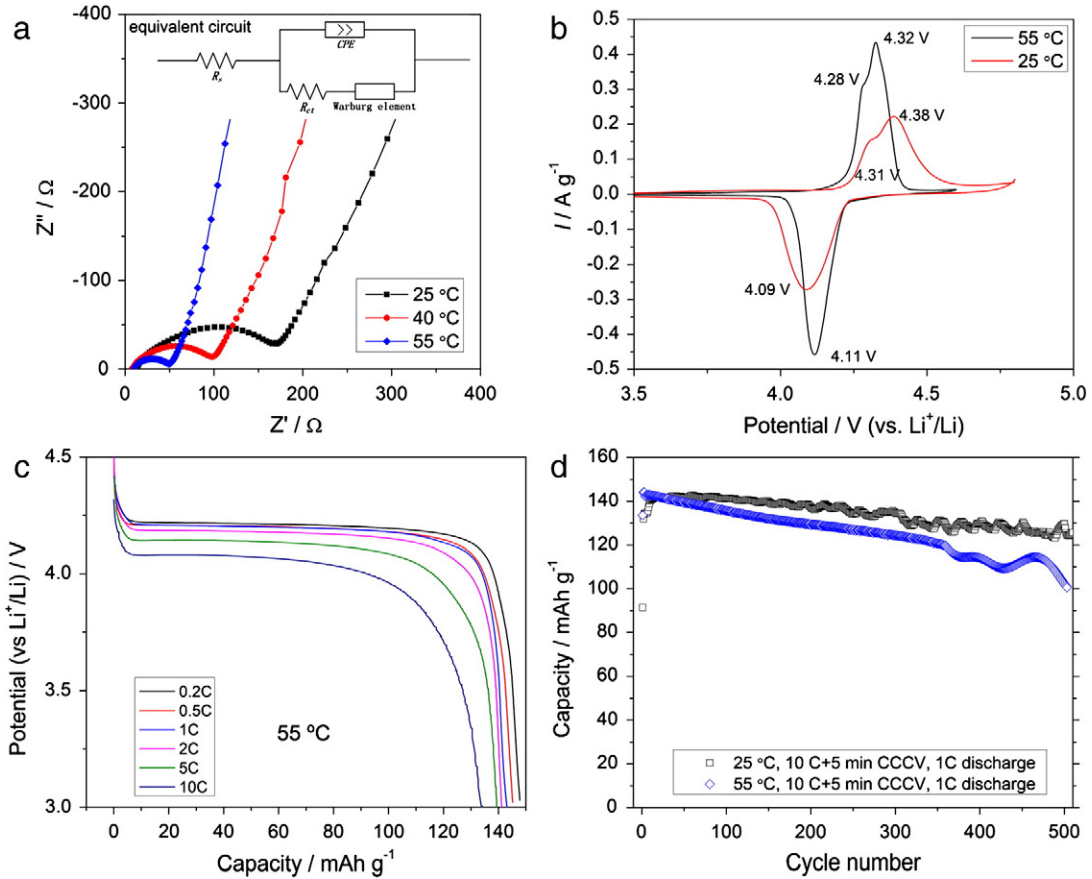


Fig. 6. Electrochemical properties of LiVPO₄F/C half-cells at elevated temperatures. (a) Nyquist-plot of EIS at 25 °C, 40 °C and 55 °C, (b) cyclic voltammetry at 25 °C and 55 °C, (c) discharge rate capabilities at 55 °C, and (d) cyclic performance at 55 °C.

~6 min, respectively. Thereafter, the cells were discharged at a relatively low rate of 1 C. For the cell charged for 2 min at constant voltage, the maximum capacity was ~120 mA h g⁻¹, and ~100 mA h g⁻¹ capacity could be retained after 500 cycles. For the cell charged at constant voltage for 5 min, the capacity at first increased and reached the maximum of ~140 mA h g⁻¹ after a few cycles of “activation”. After 500 cycles, the half-cell could still discharge a capacity of ~130 mA h g⁻¹, 93% of its maximum capacity.

As indicated in the conductivity analysis, the ionic conductivity of LiVPO₄F subsides in the temperature range of 30–90 °C, which may affect battery performances in practical applications. In addition, the stability of electrolyte with this high potential cathode is also questionable at elevated temperature. To clarify these problems, electrochemical properties of LiVPO₄F/C half-cells at reasonably elevated temperatures (40 and 55 °C) were characterized and shown in Fig. 6. As shown in the Nyquist plots of EIS Fig. 6(a), the charge-transfer resistance reduces with the increasing temperature from 25 °C to 55 °C. As shown in the CV profiles of Fig. 6(b), the cathodic and anodic peaks are also much sharper with smaller peak separation at 55 °C. The specific capacity and discharge capability at 55 °C are both slightly better than those at 25 °C. The voltage plateaus at high current rates (5 C and 10 C) are also noticeably higher owing to the reduced polarization. The enhanced electrochemical properties at elevated temperature can be ascribed to the increased electronic conductivity, boosted electrolyte fluidity/conductivity and enhanced surface activity. In general, the decrease in ionic conductivity has no obvious adverse effects on the electrochemical properties of LiVPO₄F/C in practice.

The cyclic tests were carried out following exactly the same CCCV protocol as at room temperature. The maximum capacity was of 144 mA h g⁻¹, slightly higher than that obtained at room temperature. The capacity fading is more significant at 55 °C. After 500 cycles,

the cell retained a discharge capacity of 101 mA h g⁻¹, corresponding to 70% of the maximum capacity. It is normal the cyclability of the high potential cathodes abates at elevated temperature due to the deteriorated electrolyte degradation. As a 4 V-class cathode, LiVPO₄F/C still offers a decent cyclic performance at 55 °C when compared to LiMn₂O₄ and LiMnPO₄.

3.3. Li^+ extraction/insertion behavior

As shown in Fig. 5(a), the flat discharge plateau evidently reflects a simple biphasic reaction similar to LiFePO₄/FePO₄, while the two distinct charge plateaus imply a different mechanism for the extraction of Li^+ . This phenomenon has been considered to be caused by the different energy states of split Li^+ sites in LiVPO₄F lattice [7]. The fraction of the capacity contributed from the first charge plateau is ~0.25 for the pure LiVPO₄F and ~0.4 for the LiVPO₄F/C composite in this work, while it is ~0.3 for LiVPO₄F/C in previous reports [7,15]. In addition, LiVPO₄F synthesized via sol-gel method shows only one charge plateau probably due to low crystallinity and small grain size [24]. On the other hand, LiVPO₄F synthesized via ion exchange from NaVPO₄F has two discharge plateaus in addition to the two charge plateaus [25]. These facts suggest that the Li^+ extraction/insertion mechanisms in LiVPO₄F may greatly depend on grain size, crystal structure and synthesis route.

Chemical potential differences between the two domains in Li^+ extraction were examined using cyclic voltammetry (CV) and quasi-equilibrium open circuit potential (OCP). Fig. 7(a) shows the CV curves of the LiVPO₄F/C composite and pure LiVPO₄F recorded at room temperature. Both materials show similar cathodic and anodic peaks. For the LiVPO₄F/C composite, sharp anodic peaks at 4.380 V and 4.309 V correspond to two oxidization reactions with a potential

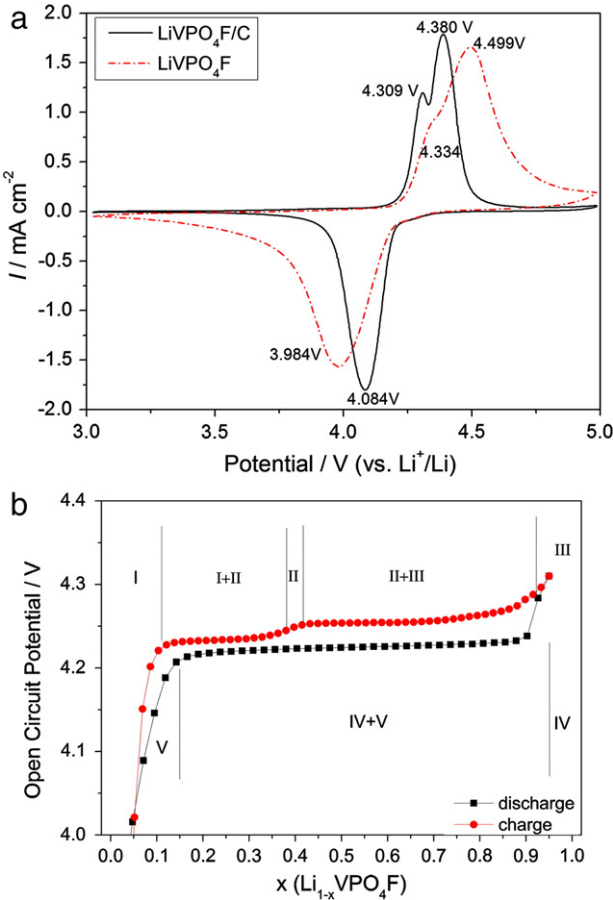


Fig. 7. (a) Cyclic voltammetry of LiVPO₄F at a sweep rate of 0.2 mV s⁻¹ at room temperature, and (b) open circuit potential (OCP) of Li_{1-x}VPO₄F as a function of extraction and insertion level x.

difference of ~70 mV, whereas only one sharp cathodic peak at 4.084 V was observed in the Li⁺ insertion process. Fig. 7(b) shows the quasi-equilibrium open circuit potential (OCP) of Li_{1-x}VPO₄F (0 ≤ x ≤ 1) obtained from GITT. In the Li⁺ extraction process, OCP

remains almost constant at about 4.234 V from x ~0.1 to ~0.4, and at about 4.254 V from x ~0.4 to ~0.9, indicating an OCP difference of ~20 mV between the two domains. Moreover, the OCP profile at x ~0.4 in extraction process shows a single-phase behavior, implying a third phase Li_xVPO₄F ($\gamma \sim 0.6$ for LiVPO₄F/C) in addition to lithium-poor VPO₄F and lithium-rich LiVPO₄F. Therefore, the Li⁺ extraction process can be divided into two stages of biphasic reactions, LiVPO₄F → Li_{0.6}VPO₄F (reaction A) and Li_{0.6}VPO₄F → VPO₄F (reaction B). In the Li⁺ insertion process, OCP remains constant at ~4.225 V, confirming a simple biphasic reaction of VPO₄F → LiVPO₄F (reaction C).

Fig. 8 shows ex-situ XRD patterns of Li_{1-x}VPO₄F electrodes at different Li⁺ extraction/embedding levels. Two distinct phases, namely pristine LiVPO₄F and lithium-poor VPO₄F can be observed from the XRD spectra. In the first stage of Li⁺ extraction when x < 0.4 in Li_{1-x}VPO₄F, only reflections from LiVPO₄F were observed, implying a minor change in crystal structure. Reflections from the VPO₄F phase (space group: C 2/c) starts to appear from x > 0.4 in the second stage of Li⁺ extraction, where both LiVPO₄F and VPO₄F coexist. As Li⁺ extraction proceeds, intensities of LiVPO₄F reflections reduce gradually accompanying with the increase intensity of the VPO₄F reflections. LiVPO₄F phase completely disappeared at a “fully” charged state (x ~ 1). The structural evolution during extraction is a possible reason for the potential difference between the two charge plateaus. Reflections from both VPO₄F and LiVPO₄F were both observed during the whole Li⁺ insertion process, indicating a simple VPO₄F/LiVPO₄F biphasic reaction. Intensities of VPO₄F reflections simply decay with Li⁺ insertion process until the complete transformation to LiVPO₄F.

3.4. Li⁺ diffusion coefficient

Li⁺ diffusion coefficients of Li_{1-x}VPO₄F in different Li⁺ extraction/embedding stages and in different phases were comprehensively studied using GITT, EIS and CV techniques. The LiVPO₄F/C composite were adopted in this study because of its superior electrochemical activity. In the electrochemical study of diffusion coefficients, it is essential and crucial to accurately estimate the active contact surface area, S, between electrode and electrolyte. To remove the error from residual carbon, the LiVPO₄F/C powder was heated at 500 °C for 10 min prior to the Brunauer–Emmett–Teller (BET) measurement. XRD results confirmed that the leftover LiVPO₄F still kept the structure of favorite without oxidation. Herein, S was determined to be 1.18 m² g⁻¹ for active LiVPO₄F based on BET measurement.

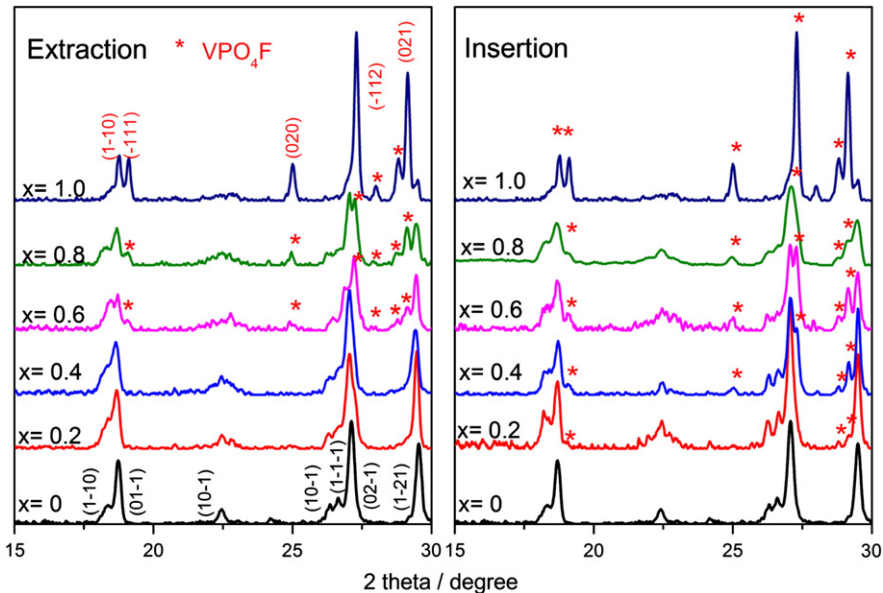


Fig. 8. Ex-situ XRD of Li_{1-x}VPO₄F electrode at different Li⁺ extraction and insertion levels.

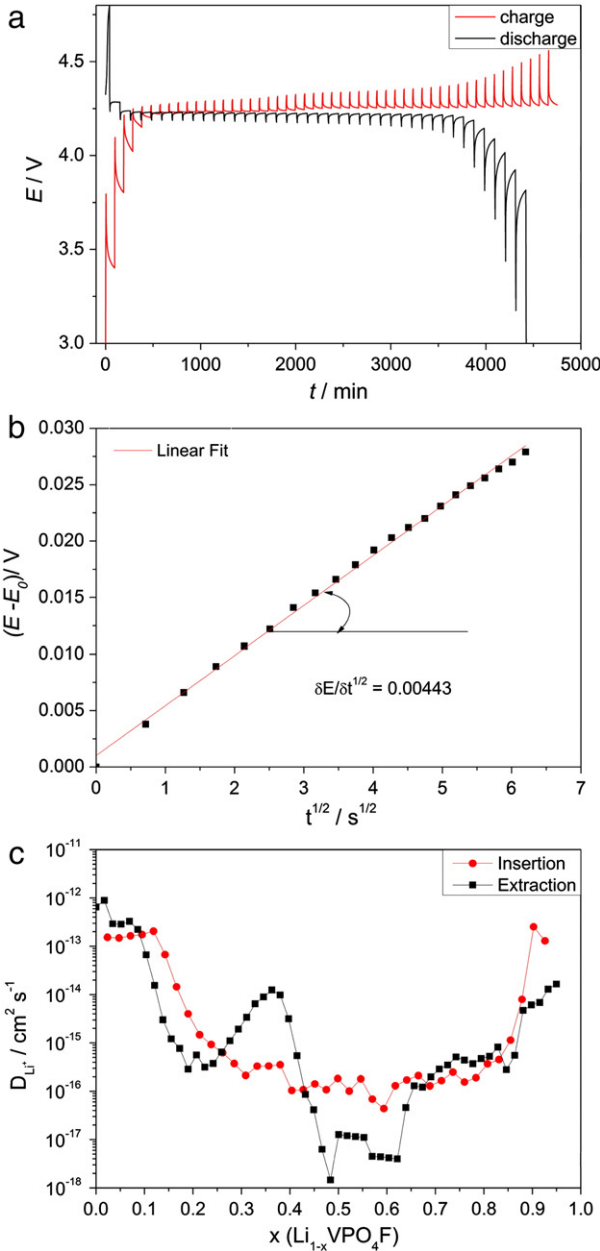


Fig. 9. (a) Charge/discharge voltage-time profiles of GITT (b) an example of titration curve at $x \sim 0.5$ (c) D_{GITT} of $\text{Li}_{1-x}\text{VPO}_4\text{F}$ as a function of x .

3.4.1. Galvanostatic intermittent titration technique

GITT was widely used to evaluate the diffusion coefficient (D_{GITT}) of electrode materials. Diffusion coefficient of lithium ions can be calculated based on Eq. (1) developed by Weppner et al. [26]:

$$D_{\text{Li}^+} = \frac{4}{\pi} \left(\frac{V_M}{SF} \right)^2 \left(I_0 \frac{\delta E_s / \delta x}{\delta E / \delta t^{1/2}} \right)^2 \quad \text{at } t \ll \tau \quad (1)$$

where V_M is molar volume ($5.2346 \times 10^{-5} \text{ m}^3 \text{ mol}^{-1}$), S is the electrode surface area ($1.18 \text{ m}^2 \text{ g}^{-1}$), F is the Faraday's constant ($96,485.3365 \text{ C mol}^{-1}$), I_0 is the pulse current (0.0375 A g^{-1}), $\delta E_s / \delta x$ is the slope of equilibrium open circuit potential versus lithium content which can be obtained from the differential of OCP curve shown in Fig. 7(b), and $\delta E / \delta t^{1/2}$ is the slope of initial transient voltage change versus square root of time. Fig. 9(b) shows an example of initial transient voltage change of E vs. $t^{1/2}$ plot recorded for $\text{Li}_{0.5}\text{VPO}_4\text{F}$ during insertion process. As can be seen, the transient voltage E exhibits a linear behavior

versus square root of time in the first 60 s. The experimental data points can be linearly fitted with a slope of $\delta E / \delta t^{1/2} = 0.00443 \text{ V s}^{-1}$. Fig. 9(c) shows the Li^+ diffusion coefficients calculated using Eq. (1) as a function of lithium content in $\text{Li}_{1-x}\text{VPO}_4\text{F}$. The calculated Li^+ diffusion coefficients D_{GITT} vary from $\sim 10^{-18} \text{ cm}^2 \text{ s}^{-1}$ to $\sim 10^{-12} \text{ cm}^2 \text{ s}^{-1}$ with different values of x in disordered "W" and "U" shapes for extraction and insertion, respectively, similar to reports on other electrode materials [27–29].

3.4.2. Electrochemical impedance spectroscopy

EIS was also used to study lithium diffusion behavior of $\text{Li}_{1-x}\text{VPO}_4\text{F}$ at different extraction/embedding level x , with a step of $x \sim 0.1$. Fig. 10(a) shows Nyquist plots of $\text{Li}_{1-x}\text{VPO}_4\text{F}$ in various extraction and insertion stages. In the low frequency range, the impedance behavior is mainly driven by diffusion in bulk electrode material or so-called Warburg impedance rather than charge transfer at interfaces. Therefore, the

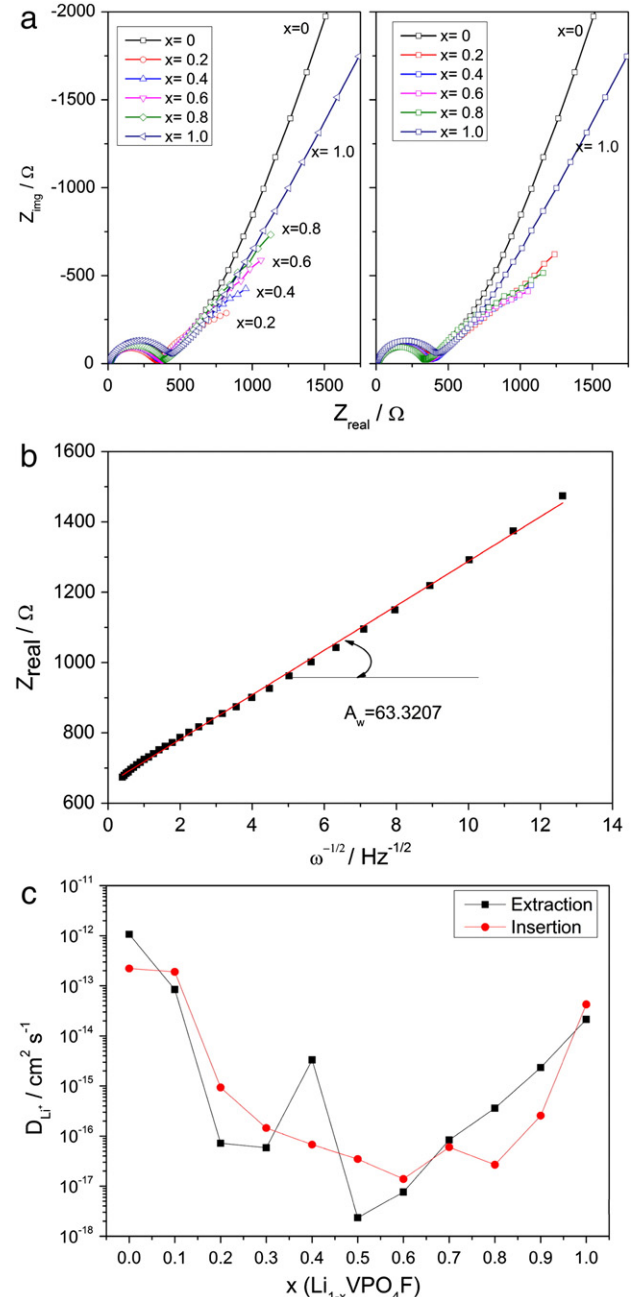


Fig. 10. (a) Nyquist plots of $\text{Li}_{1-x}\text{VPO}_4\text{F}/\text{Li}$ half-cell; (b) Z_{real} vs. $\omega^{-1/2}$ at the extraction level of $x \sim 0.5$ at low frequency range; (c) D_{EIS} of $\text{Li}_{1-x}\text{VPO}_4\text{F}$ as a function of x .

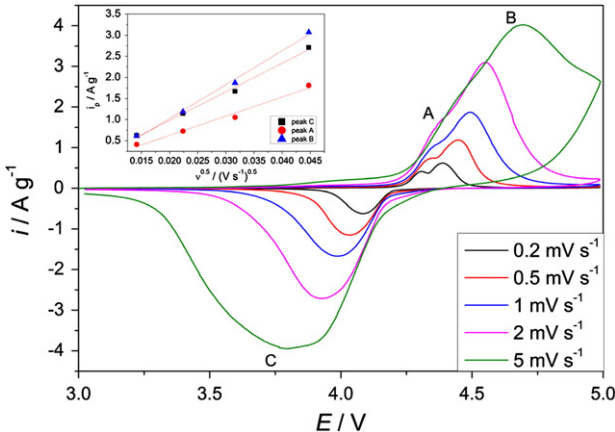


Fig. 11. Cyclic voltammetry of LiVPO₄F half-cell with different sweep rates. Inset shows the linear relationship between peak currents and square root of sweep rates.

diffusion coefficient can be calculated using Eq. (2) developed by Ho et al. [30]:

$$D_{Li^+} = \frac{1}{2} \left(V_M \frac{\delta E_s / \delta x}{SFA_w} \right)^2 \quad (2)$$

where V_M is molar volume, S is the specific electrode surface area, F is the Faraday's constant, $\delta E_s / \delta x$ is slope of equilibrium OCP versus lithium content and A_w is known as Warburg factor. A_w can be obtained from the linear relationship of Z_{real} or $-Z_{img}$ versus inverse square root of angular frequency $\omega^{-1/2}$ in the low frequency region. One of the examples is shown in Fig. 10(b) revealing a good linear relationship between Z_{real} and $\omega^{-1/2}$ of Li_{0.5}VPO₄F in low frequency range. Li⁺ diffusion coefficients of Li_{1-x}VPO₄F at different extraction or insertion levels were finally calculated using Eq. (2). The calculated diffusion coefficients D_{EIS} are also in the range from $\sim 10^{-18}$ to $\sim 10^{-12}$ cm² s⁻¹ with a similar variation trend as that derived from GITT measurement.

3.4.3. Cyclic voltammetry

Fig. 11 shows CV profiles of the LiVPO₄F/C electrode with different voltage sweep rates from 0.2 mV s⁻¹ to 5 mV s⁻¹. If the lithium

diffusion within electrode is the limiting factor rather than charge transfer across interfaces, Li⁺ diffusion coefficient can be determined by Eq. (3) [31]:

$$i_p = 0.4463 \left(\frac{F^3}{RT} \right)^{1/2} n^{3/2} S D^{1/2} C_0^* v^{1/2} \quad (3)$$

where i_p is the peak current, F is Faraday's constant, R is the molar gas constant ($8.314472 \text{ m}^2 \text{ kg s}^{-2} \text{ K}^{-1} \text{ mol}^{-1}$), T is the absolute temperature, n is the number of electrons involved in the electrochemical reaction, S is the electrode surface area, D is Li⁺ diffusion coefficient, C_0^* is the initial Li⁺ concentration and v is the sweep rate. Initial concentration of lithium ions was calculated to be $1.903 \times 10^4 \text{ mol m}^{-3}$ according to refined LiVPO₄F cell volume (174.6 \AA^3). The inset of Fig. 9 shows linear relationships between peak currents and the square root of sweep rates. Hence, apparent diffusion coefficients corresponding to three electrochemical reactions can be calculated: $D_{app}(A) = 5.6 \times 10^{-13} \text{ cm}^2 \text{ s}^{-1}$, $D_{app}(B) = 1.8 \times 10^{-12} \text{ cm}^2 \text{ s}^{-1}$ and $D_{app}(C) = 1.3 \times 10^{-12} \text{ cm}^2 \text{ s}^{-1}$. $D_{app}(A)$ of anodic reaction A was lower than $D_{Li^+}(B)$ of anodic reaction B, implying relatively inferior diffusion kinetics during the first Li⁺ extraction domain.

3.4.4. Discussion on D_{Li^+} with phase transformation

As shown above, diffusion coefficient values in biphasic domains obtained from both GITT and EIS technique are significantly lower by up to 6 orders than those measured in single phase domains. This is because GITT and EIS were developed based on several idealizations and assumptions with Frumkin isotherm model without consideration of interphase strain-stress, phase boundary movement and interphase mobility in phase transition materials. It is apparent to find that $\delta E_s / \delta x$ in Eqs. (1) and (2) approximate zero in the biphasic domain, where the equilibrium potential OCP is almost constant with x . Therefore, the calculated diffusion coefficients are much smaller in biphasic domain. This problem has been addressed by some recent reports with attempts to include phase transition kinetics into the calculation [32,33]. However, diffusion coefficients are still well estimated for each phase in single-phase domains, while the diffusion behavior in biphasic domain can be derived from those in the two phases. Hence, diffusion coefficients calculated in single-phase domain are of higher significance.

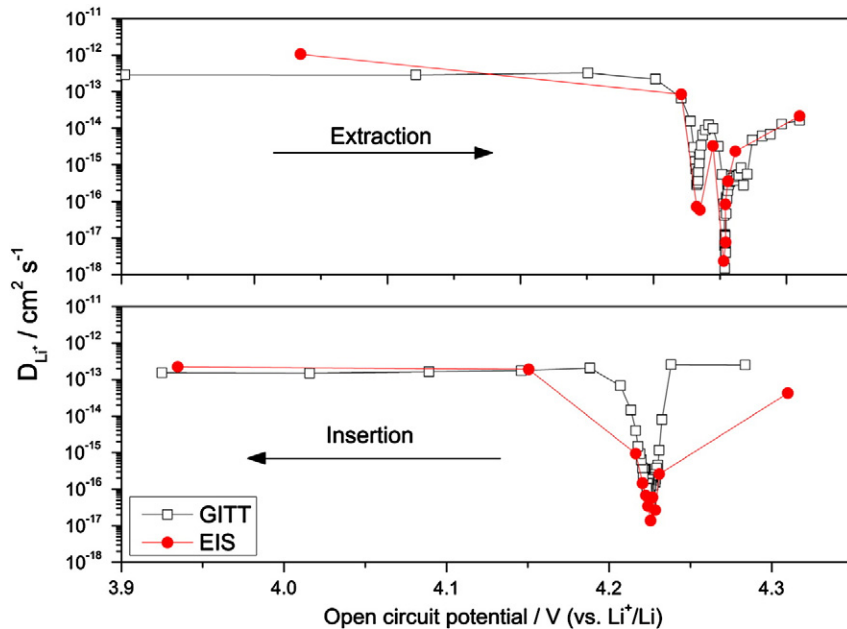


Fig. 12. Comparison of diffusion coefficients calculated through GITT and EIS as a function of OCP.

Fig. 12 compares diffusion coefficients measured using GITT and EIS as a function of quasi-equilibrium OCP. As can be seen, D_{EIS} and D_{GITT} are in very good agreement with each other. The calculated diffusion coefficients are almost constant with lithium content x in each single-phase domain. D_{Li} of lithium rich LiVPO₄F is in the range of 1.5×10^{-13} – $1.1 \times 10^{-12} \text{ cm}^2 \text{ s}^{-1}$, while D_{Li} of lithium poor VPO₄F phase is in the range of 2.1×10^{-14} – $2.5 \times 10^{-13} \text{ cm}^2 \text{ s}^{-1}$. D_{Li} of Li_{0.6}VPO₄F is the lowest 3.3×10^{-15} – $1.2 \times 10^{-14} \text{ cm}^2 \text{ s}^{-1}$ compared to the other two phases. D_{app} ($\sim 10^{-12} \text{ cm}^2 \text{ s}^{-1}$) measured from CV were slightly higher than D_{GITT} and D_{EIS} but less than one order. In general, the diffusion coefficient of LiVPO₄F (10^{-13} – $10^{-12} \text{ cm}^2 \text{ s}^{-1}$, lithium rich phase, this work) was 2 orders higher than that of olivine LiFePO₄ (10^{-15} – $10^{-14} \text{ cm}^2 \text{ s}^{-1}$ [29]), indicating a facile Li⁺ diffusion in tavorite lattice. This is also consistent with the results of bulk conductivity in this work.

4. Conclusion

In summary, tavorite LiVPO₄F is a highly active cathode material with a relatively fast ionic transport and a pleasant 4.2 V potential vs. Li⁺/Li. The electrical conductivity of tavorite LiVPO₄F is $8.1 \times 10^{-7} \text{ S cm}^{-1}$ at room temperature, while the electronic conductivity is only $\sim 10^{-11} \text{ S cm}^{-1}$. Harsh control of particle size may not be necessary to achieve high rate capabilities owing to the fast ionic conductivity, whereas electronic insulation may be the main bottleneck for charge transport. This challenge can be tackled through carbon coating as demonstrated in this work. LiVPO₄F/C composite with a mean particle size of $\sim 200 \text{ nm}$ exhibits impressive discharge/charge capability and good cyclability at both room temperature and elevated temperature (55 °C). Li⁺ extraction from tavorite LiVPO₄F consists of two serial phase-transitions of LiVPO₄F \rightarrow Li_{0.6}VPO₄F \rightarrow VPO₄F. Li⁺ diffusion coefficient in lithium rich phase LiVPO₄F is 10^{-13} – $10^{-12} \text{ cm}^2 \text{ s}^{-1}$. The intermediate phase Li_{0.6}VPO₄F in extraction seems to have a relatively inferior Li⁺ diffusion coefficient ($\sim 10^{-15} \text{ cm}^2 \text{ s}^{-1}$), which may be another limiting factor for the thorough and fast extraction of Li⁺. It is interesting to note that the temperature dependence of electrical conductivity in bulk LiVPO₄F follows an abnormal non-Arrhenius relationship, which can certainly trigger further in-depth characterization and simulation.

Acknowledgment

This work was supported by Singapore Energy Market Authority through the grant R-265-000-371-490 (EPD090005RFP(A)) and National University of Singapore.

References

- [1] P. Barpanda, K. Djellab, N. Recham, M. Armand, J.M. Tarascon, *J. Mater. Chem.* 21 (27) (2011) 10143.
- [2] J.M. Tarascon, N. Recham, M. Armand, J.N. Chotard, P. Barpanda, W. Walker, L. Dupont, *Chem. Mater.* 22 (3) (2010) 724.
- [3] N. Recham, J.N. Chotard, L. Dupont, C. Delacourt, W. Walker, M. Armand, J.M. Tarascon, *Nat. Mater.* 9 (1) (2010) 68.
- [4] P. Barpanda, N. Recham, J.N. Chotard, K. Djellab, W. Walker, M. Armand, J.M. Tarascon, *J. Mater. Chem.* 20 (9) (2010) 1659.
- [5] T.N. Ramesh, K.T. Lee, B.L. Ellis, L.F. Nazar, *Electrochem. Solid-State Lett.* 13 (4) (2010) A43.
- [6] N. Recham, J.N. Chotard, J.C. Jumas, L. Laffont, M. Armand, J.M. Tarascon, *Chem. Mater.* 22 (3) (2009) 1142.
- [7] J. Barker, M.Y. Saidi, J.L. Swoyer, *J. Electrochem. Soc.* 150 (10) (2003) A1394.
- [8] A.K. Padhi, K.S. Nanjundaswamy, J.B. Goodenough, *J. Electrochem. Soc.* 144 (4) (1997) 1188.
- [9] C. Delacourt, L. Laffont, R. Bouchet, C. Wurm, J.B. Leriche, M. Morcrette, J.M. Tarascon, C. Masquelier, *J. Electrochem. Soc.* 152 (5) (2005) A913.
- [10] M.M. Thackeray, P.J. Johnson, L.A. de Picciotto, P.G. Bruce, J.B. Goodenough, *Mater. Res. Bull.* 19 (2) (1984) 179.
- [11] R. Koksbang, J. Barker, H. Shi, M.Y. Saidi, *Solid State Ionics* 84 (1–2) (1996) 1.
- [12] M. Pivko, M. Bele, E. Tchernychova, N.Z. Logar, R. Dominko, M. Gaberscek, *Chem. Mater.* 24 (6) (2012) 1041.
- [13] R.K.B. Gover, P. Burns, A. Bryan, M.Y. Saidi, J.L. Swoyer, J. Barker, *Solid State Ionics* 177 (26–32) (2006) 2635.
- [14] F. Zhou, X. Zhao, J.R. Dahn, *Electrochem. Commun.* 11 (3) (2009) 589.
- [15] M.V. Reddy, G.V. Subba Rao, B.V.R. Chowdari, *J. Power. Sources* 195 (17) (2010) 5768.
- [16] J. Barker, R.K.B. Gover, P. Burns, A. Bryan, M.Y. Saidi, J.L. Swoyer, *J. Electrochem. Soc.* 152 (9) (2005) A1776.
- [17] A.C. Larson, R.B. Von Dreele, Los Alamos National Laboratory Report LAUR, 1994. 86.
- [18] B.H. Toby, *J. Appl. Crystallogr.* 34 (2001) 210.
- [19] J. Barker, R.K.B. Gover, P. Burns, A. Bryan, M.Y. Saidi, J.L. Swoyer, *J. Power. Sources* 146 (1–2) (2005) 516.
- [20] K. Momma, F. Izumi, *J. Appl. Crystallogr.* 44 (6) (2011) 1272.
- [21] M.H. Hebb, *J. Chem. Phys.* 20 (1952) 185.
- [22] Y. Takahashi, Y. Gotoh, J. Akimoto, S. Mizuta, K. Tokiwa, T. Watanabe, *J. Solid State Chem.* 164 (1) (2002) 1.
- [23] M. Nishizawa, T. Ise, H. Koshika, T. Itoh, I. Uchida, *Chem. Mater.* 12 (5) (2000) 1367.
- [24] Y.Z. Li, Z. Zhou, X.P. Gao, J. Yan, *J. Power. Sources* 160 (1) (2006) 633.
- [25] J. Barker, M.Y. Saidi, J.L. Swoyer, *J. Electrochem. Soc.* 151 (10) (2004) A1670.
- [26] W. Weppner, R.A. Huggins, *J. Electrochem. Soc.* 124 (10) (1977) 1569.
- [27] D. Aurbach, M.D. Levi, E. Levi, H. Teller, B. Markovsky, G. Salitra, U. Heider, L. Heider, *J. Electrochem. Soc.* 145 (9) (1998) 3024.
- [28] M.D. Levi, D. Aurbach, *Electrochim. Acta* 45 (1–2) (1999) 167.
- [29] P.P. Prosin, M. Lisi, D. Zane, M. Pasquali, *Solid State Ionics* 148 (1–2) (2002) 45.
- [30] C. Ho, I.D. Raistrick, R.A. Huggins, *J. Electrochem. Soc.* 127 (2) (1980) 343.
- [31] A.J. Bard, L.R. Faulkner, *Electrochemical Methods: Fundamentals and Applications*, Wiley, 2000.
- [32] Y. Zhu, C. Wang, *J. Phys. Chem. C* 114 (6) (2010) 2830.
- [33] M.D. Levi, D. Aurbach, *J. Solid State Electrochem.* 11 (8) (2007) 1031.